A Third-Order Bandpass Three-Dimensional Frequency Selective Surface with Multiple Transmission Zeros

Zhengyong Yu[*1, 2] and Wanchun Tang[2]

[1] School of Computer and Communication Engineering
Huai'an Vocational College of Information Technology, Huai'an, 223003, China
yonglly@sina.com

[2] School of Physics and Technology
Nanjing Normal University, Nanjing, 210023, China
eewctang@njnu.edu.cn

Abstract ─ We present a third-order bandpass three-dimensional frequency selective surface (3D FSS) with multiple transmission zeros in this paper. The unit cell of the proposed 3D FSS consists of an air-filled square waveguide and a cuboid dielectric block with three concentric metallic square loops. Due to its inner electromagnetic coupling in the unit cell, this FSS provides a flat passband with three transmission poles, a wide out-of-band rejection with three transmission zeros, and high frequency selectivity. In order to explain the working principle, an equivalent circuit model is established and investigated. Finally, an FSS prototype is fabricated and measured, and the results exhibit good stability for both TE and TM polarizations under incident angles from 0° to 50°. Besides, this FSS has a relatively compact unit cell.

Index Terms ─ Bandpass, dual polarizations, frequency selective surface (FSS), third-order, transmission zeros.

I. INTRODUCTION

During the past decade, frequency selective surfaces (FSSs) have been widely studied due to their superior spatial filtering characteristics for some practical applications, including radar cross section reduction, electromagnetic interference shielding and so on [1-5]. Recently, FSSs are also used as partially reflecting surfaces with aperture antenna to drastically improve their radiation patterns and antennas performance [6]. Typical FSSs are usually two-dimensional (2D) arrays assembled by periodically arranged planar unit cells, which can exhibit bandpass or bandstop filtering responses. For the bandpass FSS, it requires flat transmission response with low insertion loss within the passband, as well as fast roll-off and wide rejection out of the passband. Besides, it should also have dual polarizations, good angular stability and compact unit

cell.

To meet these above requirements, many second-order bandpass FSSs have been reported [7-12]. A bandpass FSS with second-order response is proposed by inserting the capped dielectric in the perforated metallic plate [7]. However, this FSS suffers from slow roll-off out of the passband without any transmission zero, resulting in poor frequency selectivity. To achieve fast roll-off filtering performance, a bandpass FSS is designed by using vertically cascaded substrate integrated waveguide (SIW) cavities [8]. In such an FSS, two transmission zeros located near the edges of the passband are generated by the coupling between multiple resonant modes in these SIW cavities. However, the angular stability deteriorates due to its large electrical size. Then, a quasi-elliptic bandpass FSS is presented based on the hybrid array of double square loops and gridded square loops, but its electrical size and thickness are also large [9]. Moreover, three-dimensional (3D) FSSs can provide 3D resonant cavities to achieve a desired response [10-12], as an alternative method. For example, two bandpass 3D FSSs with the quasi-elliptic responses are presented, taking advantage of the shielded microstrip lines [10-11]. Unfortunately, these two designs only operate under a single polarization. Later, the authors in [12] propose a dual-polarized bandpass 3D FSS with fast both sides roll-off by the combination of the metal cylindrical pipes and disks. Nevertheless, this 3D FSS has a large electrical size and the angular stability is also needed to be improved.

For the third-order or high-order bandpass FSSs, several design approaches of these FSSs are investigated [13-19]. Two FSSs with third- and fourth-order bandpass responses are realized by using the arrays of sub-wavelength periodic structures with non-resonant elements [13]. A multilayered third-order bandpass FSS

is obtained according to the coupled matrix theory [14]. Another FSS is achieved by the two capacitive patch layers and a slot layer, exhibiting wide-passband performance [15]. However, these designs in [13-15] do not have any transmission zero, so the frequency selectivity is unsatisfactory. Then, one transmission zero located at the right side of the passband is produced for high frequency selectivity [16-18]. In [16], one FSS structure is presented by a hybrid resonator to realize a third-order bandpass response with one transmission zero. In [17-18], similar frequency selective performances are achieved based on the two capacitive patch resonators and one hybrid resonator. Additionally, one FSS with an additional transmission zero located at the left side of the passband is designed to provide a stable, highly-selective, and wide-passband response [19]. However, this design has a larger unit cell size and a poor out-of-band rejection performance. Thus, there is a challenge for the FSS design to realize flat passband, high frequency selectivity, wide out-of-band rejection, good angular stability, dual polarizations, and compact unit cell simultaneously. In addition to the above FSSs composed of printed microwave substrates, the FSSs can also be made of all-dielectric materials [20], printed surfaces [21], all-metal structures [22], and artificial magnetic conductor [23]. Besides, one new approach in designing bandpass FSSs is proposed by using artificial intelligence in conjunction with an electromagnetic simulator [24].

In this paper, a dual-polarized bandpass 3D FSS is presented to obtain these performances simultaneously. The unit cell of the proposed 3D FSS is composed of an air-filled square waveguide and a cuboid dielectric block with three concentric metallic square loops. By the inner electromagnetic coupling in the unit cell, this FSS realizes a third-order bandpass response with wide out-of-band rejection and high frequency selectivity. Meanwhile, its frequency selectivity is further improved by the high quality factor (Q-factor) of the square waveguide cavity. An equivalent circuit model is established and analyzed to explain its working principle. At last, a prototype of the proposed 3D FSS is fabricated and measured, and its simulated results are coincided with experimental ones.

II. UNIT CELL DESIGN AND SIMULATION

As depicted in Fig. 1 (a), the unit cell of the proposed 3D FSS consists of an air-filled square waveguide, and a cuboid dielectric block with three concentric metallic square loops is inserted in the square waveguide. As shown in Fig. 1 (b), the gridded square loop (GSL) structures can be observed on both the top and bottom layers of the unit cell. The periods of the unit

cell along the x- and y-axes are denoted as p. The wall thickness and height of the square waveguide are t and h. These two metallic square loops etched on the top and bottom layers have the same geometrical parameters with the size l_1 and width w_1. The size and width of the square loop in the middle layer are l_2 and w_2. The relative dielectric constant of the cuboid dielectric block is expressed as ε_r.
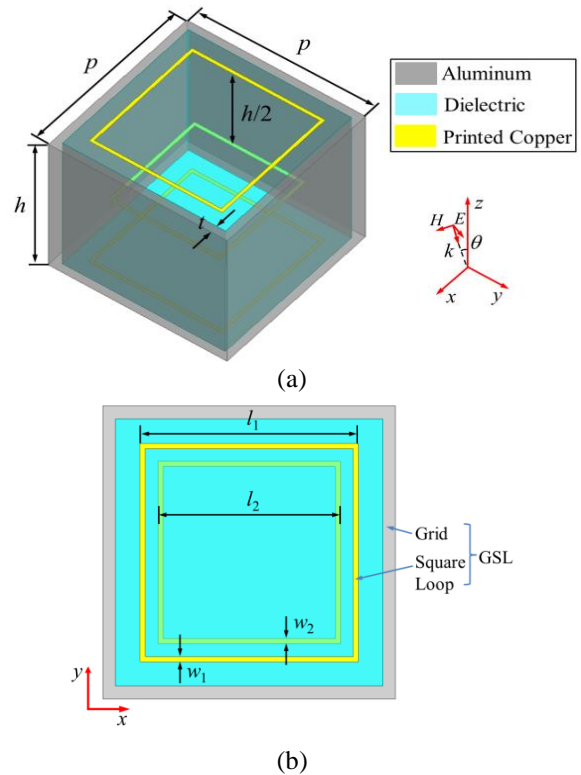

(a)

(b)

Fig. 1. Unit cell of the proposed 3D FSS. (a) Perspective view and (b) top view.

Figure 2 gives the simulated frequency responses of the proposed 3D FSS under normal incidence by the commercial ANSYS HFSS Simulation Software. The design parameters of the proposed 3D FSS are listed in Table 1. It can be observed from Fig. 2 a third-order bandpass response with wide out-of-band rejection and high frequency selectivity is achieved, including three transmission poles f_{p1}=5.46 GHz, f_{p2}=5.74 GHz and f_{p3}=5.87 GHz in the passband, and three transmission zeros f_{z1}=6.08 GHz, f_{z2}=6.35 GHz and f_{z3}=7.1 GHz in the upper stopband. The master and slave boundary conditions are applied for the unit cell simulations with Floquet ports, as depicted in Fig. 3.

For expressing the fractional bandwidths of the passband and the upper stopband, FBW$_{3dB}$ and FBW$_{20dB}$ are defined as follows:

$$FBW_{3dB} = \frac{Bandwidth\ of\ |S_{21}| \geq -3dB}{Center\ frequency\ of\ the\ passband\ (f_1)} \times 100\%,\quad (1)$$

$$FBW_{20dB} = \frac{Bandwidth\ of\ |S_{21}| \leq -20dB}{Center\ frequency\ of\ the\ upper\ stopband\ (f_2)} \times 100\%.\quad (2)$$

The simulated 3 dB bandwidth of the passband is 0.61 GHz (5.3-5.91 GHz), and the center frequency of the passband (f_1) is 5.605 GHz. The simulated 20 dB bandwidth of the upper stopband is 2.7 GHz (5.99-8.69 GHz), and the center frequency of the upper stopband (f_2) is 7.34 GHz. Therefore, FBW_{3dB} and FBW_{20dB} are 10.9% and 36.8%, respectively.

Table 1: Design parameters of the proposed 3D FSS

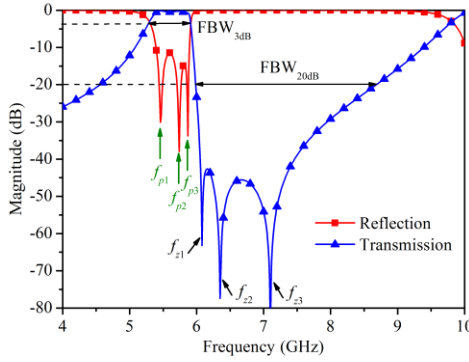| p	l_1	l_2	w_1
11.4 mm	8.5 mm	7.1 mm	0.2 mm
w_2	h	t	ε_r
0.2 mm	10 mm	0.5 mm	3.5

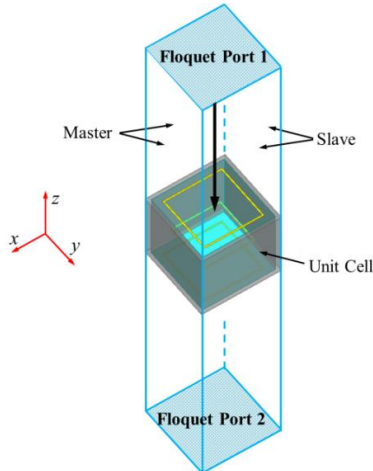Fig. 2. Simulated frequency responses of the proposed 3D FSS by HFSS.

Fig. 3. Periodic boundary conditions of the unit cell.

III. EQUIVALENT CIRCUIT MODEL

In order to explain the working principle of the proposed 3D FSS, an equivalent circuit model is established under the normal incidence and depicted in Fig. 4. The equivalent circuit model consists of five parts, including three LC resonators separated by the two square waveguides. These three LC resonators represent the GSLs at the top/bottom layers and the square loop in the middle layer. These three LC resonators are denoted as R_1, R_2 and R_3, as shown in Fig. 4 (a). The square waveguide is modeled as the transmission line with the frequency-depended characteristic impedance $Z(f)$ and electrical length $\theta/2$ under the dominant mode TE_{10}. The inductors L_0 and L_1 are the self-inductance of the grid and square loop of the GSLs, respectively, and the inductor L_2 is the self-inductance of the square loop in the middle layer. The capacitor C_1 is the gap capacitance between the square loop and the grid for the GSL. The capacitor C_2 is the gap capacitance between the square loop and waveguide inner wall, which is located in the middle layer. The electrical and magnetic couplings between R_1 and R_2 are represented by the mutual capacitance C_m and the mutual inductance L_m, whereas the electrical and magnetic couplings between the R_3 and R_1/R_2 are denoted by the mutual capacitance C_{m1} and the mutual inductance L_{m1}. For the equivalent circuit modeling, the losses are not considered and included.
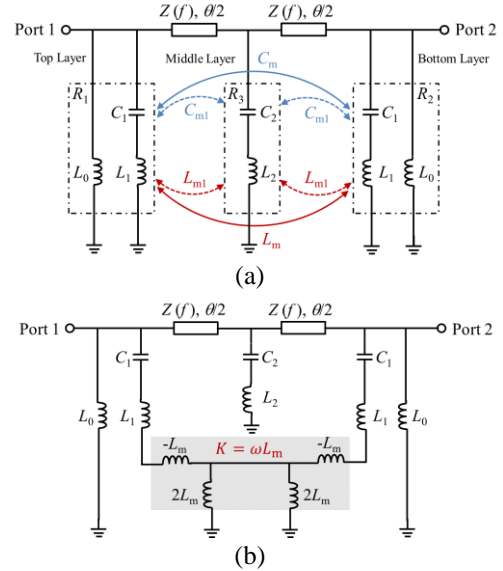

(a)

(b)

Fig. 4. Equivalent circuit model of the proposed 3D FSS. (a) General model and (b) simplified model.

For simplicity, only the magnetic coupling (L_m) between R_1 and R_2 is considered in our equivalent circuit modeling. The mutual inductance L_m can be denoted by an impedance inverter $K=\omega L_m$ [25]. Thus, a simplified circuit model is obtain and shown in Fig. 4 (b). It is observed that two propagation paths, including the coupling path through mutual inductance (L_m) and the

signal path directly through the square waveguide cavity ($Z(f)$, θ), are constructed. The electromagnetic waves are combined out-of-phase by these two paths, resulting in multiple transmission zeros at finite frequencies. The initial circuit values of the electrical parameters L_0, L_1, L_2, C_1 and C_2 can be calculated by using the given formulas in [26], and the final parameter values of the equivalent circuit model are extracted by the curve-fitting method [27], as shown in Table 2. The free space at the top and bottom layers of the unit cell can be modeled as a transmission line with the characteristic impedance of $Z_0=377$ Ω.

Table 2: Final parameter values of the equivalent circuit model

L_0	L_1	L_2
4.43 nH	5.36 nH	13.01 nH
L_m	C_1	C_2
-0.0015 nH	0.1 pF	0.0494 pF

In view of the symmetry of the equivalent circuit model shown in Fig. 4 (b), symmetric network theory is adopted to simplify the analysis of this circuit, as depicted in Fig. 5 (a). The even- and odd-mode equivalent circuits are given in Fig. 5 (b) and Fig. 5 (c) by applying an ideal magnetic wall (an open circuit) or an ideal electrical wall (a short circuit) at the symmetry plane T-T ', respectively.
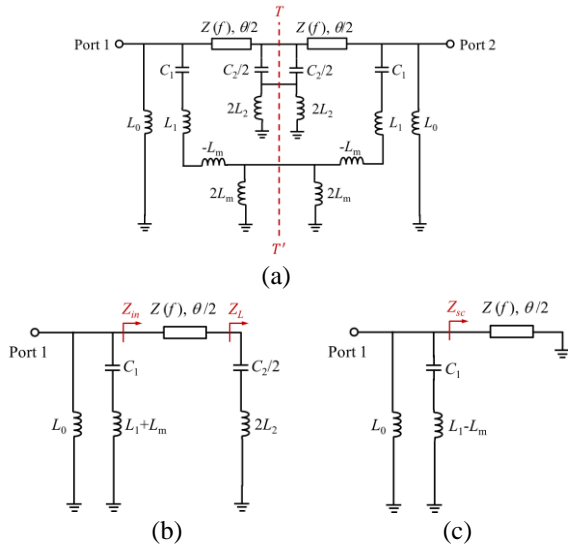

Fig. 5. Even- and odd-mode analysis method. (a) Symmetry plane T-T ', (b) even-mode circuit, and (c) odd-mode circuit.

The characteristic impedance $Z(f)$ and electrical length θ of the square waveguide transmission line are defined as [28]:

$$Z(f) = \frac{\pi^2}{8}\sqrt{\frac{\mu_0}{\varepsilon_0 \varepsilon_r}}\frac{1}{\sqrt{1-\left(\frac{\lambda(f)}{2(p-2t)}\right)^2}}, \quad (3)$$

$$\lambda(f) = \frac{1}{f\sqrt{\mu_0 \varepsilon_0 \varepsilon_r}}, \quad (4)$$

$$\theta = h\sqrt{(2\pi f)^2 \mu_0 \varepsilon_0 \varepsilon_r - \left(\frac{\pi}{p-2t}\right)^2}, \quad (5)$$

where μ_0 is the magnetic permeability of free space, and ε_0 is the electric permittivity of free space.

From Fig. 5 (b), the load impedance Z_L of the square waveguide transmission line ($Z(f)$, θ/2) is calculated by:

$$Z_L = j\omega(2L_2) + \frac{1}{j\omega\left(\frac{C_2}{2}\right)}. \quad (6)$$

Then, the corresponding input impedance Z_{in} can be expressed as:

$$Z_{in} = Z(f)\frac{Z_L + jZ(f)\tan(\theta/2)}{Z(f) + jZ_L \tan(\theta/2)}. \quad (7)$$

Consequently, the even-mode input admittance Y_{even} is represented as:

$$Y_{even} = \frac{1}{j\omega L_0} + \frac{1}{\frac{1}{j\omega C_1} + j\omega(L_1 + L_m)} + \frac{1}{Z_{in}}. \quad (8)$$

Similarly, the odd-mode input admittance Y_{odd} can be deduced from Fig. 5 (c) as follows:

$$Y_{odd} = \frac{1}{j\omega L_0} + \frac{1}{\frac{1}{j\omega C_1} + j\omega(L_1 - L_m)} + \frac{1}{Z_{sc}}, \quad (9)$$

$$Z_{sc} = jZ(f)\tan(\theta/2), \quad (10)$$

where Z_{sc} is the input impedance of the waveguide transmission line ($Z(f)$, θ/2) under a short circuit.

Finally, the scattering matrix parameters of the proposed 3D FSS can be calculated by using the following equations [25]:

$$S_{11} = S_{22} = \frac{1/Z_0^2 - Y_{even}Y_{odd}}{(1/Z_0 + Y_{even})(1/Z_0 + Y_{odd})}, \quad (11)$$

$$S_{21} = S_{12} = \frac{1/Z_0(Y_{odd} - Y_{even})}{(1/Z_0 + Y_{even})(1/Z_0 + Y_{odd})}. \quad (12)$$

Figure 6 compares the reflection and transmission coefficients obtained from HFSS and equivalent circuit model, and there is a good agreement. There is a relative difference at the upper stopband from 6 to 10 GHz, because the couplings (C_m, C_{m1}, L_{m1}) are ignored in the equivalent circuit model. Besides, the square waveguide is analyzed under the dominant mode TE$_{10}$ without considering the effect of the higher modes. However, the established equivalent circuit model can give a view of
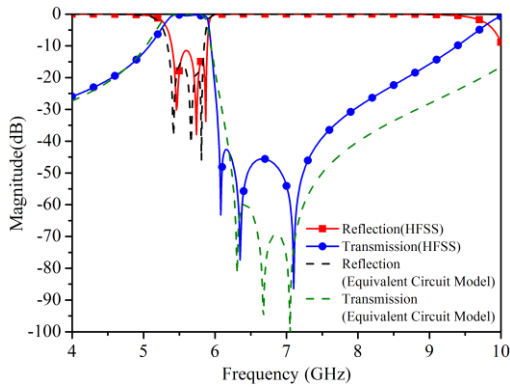
the working mechanism of the proposed 3D FSS.

Fig. 6. Comparison of the reflection and transmission coefficients by HFSS and equivalent circuit model.
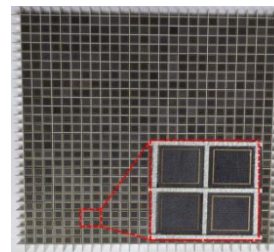
IV. FABRICATION AND MEASUREMENT

To verify the performances of the proposed 3D FSS, the prototype is fabricated. It consists of two building parts and their geometrical dimensions are given in Fig. 7 (a). The building part I is one piece of aluminium plate with a thickness of 1.0 mm, and 27 slots are periodically cut halfway along the plate. The building part II is one cuboid dielectric block with a thickness of 10 mm, and it is fabricated by using multi-layer PCB technology. The material of the dielectric block is F4B and its relative dielectric constant is 3.5 with the loss tangent of 0.005. For assembly, the pieces (building part I) are cross-joined together through the opening slots to construct an aluminium frame, which achieves the periodic square waveguides. Then, the cuboid dielectric blocks (building part II) are inserted, one by one, into the constructed frame. Finally, the size of the fabricated 3D FSS is 317.4 mm×317.4 mm with 26×26 unit cells, as shown in Fig. 7 (b). The electrical size of the unit cell $p \times p \times h$ is $0.21\lambda_0 \times 0.21\lambda_0 \times 0.187\lambda_0$, where λ_0 is the free-space wavelength at f_1.

The frequency responses of the proposed 3D FSS are measured by the free-space method, and its measurement environment is given in Fig. 7 (c). There are two wideband horn antennas (operating from 1 to 18 GHz), the FSS prototype, and the rotatable screen covered by absorbers. The FSS prototype is placed within the rectangular through-hole window in the center of the rotatable screen for measurement of incident stability. A pair of horn antennas are located about 1.2 m apart from each side of the centered rotatable screen, so that a uniform plane wave striking upon the FSS. The two horn antennas are connected by the vector network analyzer. Besides, the measurement device is surrounded by using the absorbing screens. For the transmission coefficients measurement, the propagation loss is firstly

eliminated by the normalization of the measured results without the FSS prototype, and the environment noise is eliminated by the measured results of an identically-sized metallic plate. Then, the frequency responses of proposed 3D FSS can be obtained. Besides, the time-domain gating function of the vector network analyzer is also applied to calibrate the measured results for considering the multipath effects.
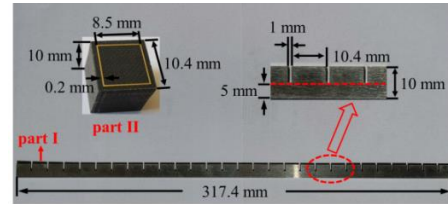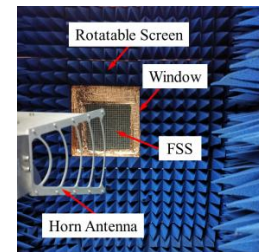
Fig. 7. Fabricated 3D FSS. (a) Building parts and dimensions, (b) photograph of the fabricated FSS prototype, and (c) measurement setup.

The measured results under different incident angles and polarizations are demonstrated in Fig. 8 compared with the simulated ones. It is clear that the transmission coefficients keep very stable versus variable incident angles up to 50° for transverse electric (TE) and transverse magnetic (TM) polarizations. The insertion loss within passband gradually becomes larger as the incident angle increases, which is mainly caused by the variation of wave impedance of the incident wave. The measured insertion loss (1.1 dB) is larger than the simulated one (0.7 dB) under the normal incidence. In addition, due to the decrease of the Q-factor for the fabricated 3D FSS, the measured 3dB bandwidth of the passband is widened. The discrepancies between the measurement and simulation result from fabrication tolerance, assembly tolerance and measurement error. Table 3 provides the comparison between the presented 3D FSS and previously reported designs with similar frequency responses, and our proposed 3D FSS exhibits good angular stability, dual polarizations, and small electrical size. However, compared with 2D FSSs composed of PCB, our designed 3D FSS suffers from the assembly process on account of a large number of building blocks.

Table 3: Comparison of the FSS designs with similar responses

| Ref.	Order	TZs Num.	Unit Cell Size and Thickness	Insertion Loss/Return Loss at f_1 (dB)	Upper Out-of-Band Rejection (dB)	Polarization	Angular Stability (TE/TM)
[7]	2	0	$0.42\lambda_0 \times 0.42\lambda_0 \times 0.14\lambda_0$	0.5/11.5	-	Dual	40°/40°
[8]	2	2	$0.72\lambda_0 \times 0.72\lambda_0 \times 0.085\lambda_0$	2.5/-	18	Dual	20°/20°
[9]	2	3	$0.3\lambda_0 \times 0.3\lambda_0 \times 0.217\lambda_0$	0.5/18	35	Dual	40°/40°
[10]	2	3	$0.16\lambda_0 \times 0.15\lambda_0 \times 0.287\lambda_0$	1.2/23	33	Single	40°
[11]	2	2	$0.32\lambda_0 \times 0.21\lambda_0 \times 0.167\lambda_0$	1.2/19	50	Single	20°
[12]	2	3	$0.65\lambda_0 \times 0.65\lambda_0 \times 0.268\lambda_0$	2.2/7.5	14	Dual	-/20°
[13]	3	0	$0.13\lambda_0 \times 0.13\lambda_0 \times 0.094\lambda_0$	0.8/14	-	Dual	45°/45°
[17]	3	1	$0.23\lambda_0 \times 0.23\lambda_0 \times 0.035\lambda_0$	0.9/-	17.5	Dual	50°/50°
[19]	3	2	$0.32\lambda_0 \times 0.32\lambda_0 \times 0.128\lambda_0$	0.72/14	25	Dual	40°/40°
This work	**3**	**3**	$\mathbf{0.21\lambda_0 \times 0.21\lambda_0 \times 0.187\lambda_0}$	**1.1/12**	**43**	**Dual**	**50°/50°**
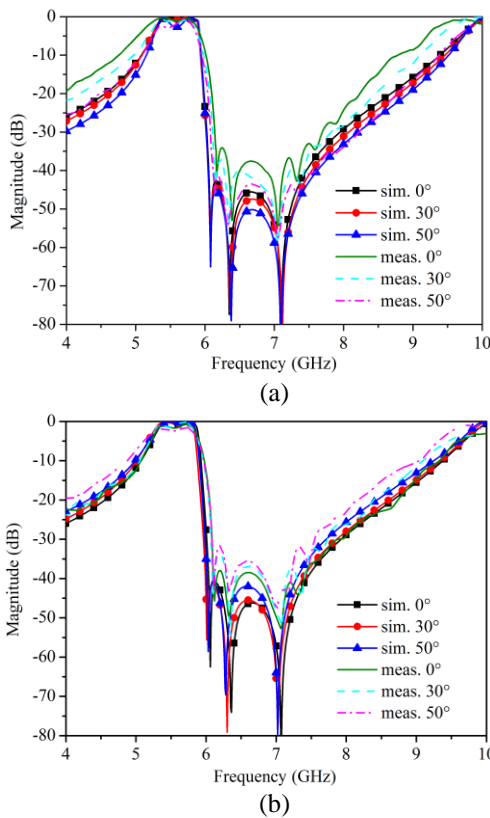
Fig. 8. Measured and simulated transmission coefficients of the proposed 3D FSS under oblique incidence for (a) TE polarization and (b) TM polarization.

V. CONCLUSION

A dual-polarized 3D FSS has been presented in this paper, which provides a third-order bandpass response with three transmission zeros. By inserting a cuboid dielectric block with three concentric metallic square loops into an air-filled square waveguide, the unit cell of the proposed 3D FSS is constructed. Due to the inner electromagnetic coupling in the unit cell, this FSS can achieve a flat passband response with wide out-of-band rejection and high frequency selectivity. The selectivity can be further improved by the high Q-factor of square waveguide cavity. An equivalent circuit model successfully demonstrates the working principle. The measured results show high consistency with the simulated ones, which verifies the performances of the proposed 3D FSS.

REFERENCES

[1] B. A. Munk, *Frequency Selective Surfaces: Theory and Design.* New York, NY, USA: Wiley, 2000.

[2] H. Huang and Z. Shen, "Low-RCS reflectarray with phase controllable absorptive frequency-selective reflector," *IEEE Trans. Antennas Propag.*, vol. 67, no. 1, pp. 190-198, 2019.

[3] H. Huang, Z. Shen, and A. A. Omar, "3-D absorptive frequency selective reflector for antenna radar cross section reduction," *IEEE Trans. Antennas Propag.*, vol. 65, no. 11, pp. 5908-5917, 2017.

[4] D. Li, T. W. Li, E. P. Li, and Y. J. Zhang, "A 2.5-D angularly stable frequency selective surface using via-based structure for 5G EMI shielding," *IEEE Trans. Electromagn. Compat.*, vol. 60, no. 3,

pp. 768-775, 2018.

[5] M. Idrees, S. Buzdar, S. Khalid, and M. A. Khalid, "A miniaturized polarization independent frequency selective surface with stepped profile for shielding applications," *Applied Computational Electromagnetics Society Journal*, vol. 31, no. 5, pp. 531-536, 2016.

[6] A. Lalbakhsh, M. U. Afzal, K. P. Esselle, S. L. Smith, and B. A. Zeb, "Single-dielectric wideband partially reflecting surface with variable reflection components for realization of a compact high-gain resonant cavity antenna," *IEEE Trans. Antennas Propag.*, vol. 67, no. 3, pp. 1916-1921, 2019.

[7] C. Jin, Q. H. Lv, J. L. Wang, and Y. Li, "Capped dielectric inserted perforated metallic plate bandpass frequency selective surface," *IEEE Trans. Antennas Propag.*, vol. 65, no. 12, pp. 7129-7136, 2017.

[8] G. Q. Luo, W. Hong, Q. H. Lai, K. Wu, and L. L. Sun, "Design and experimental verification of compact frequency-selective surface with quasi-elliptic bandpass response," *IEEE Trans. Microw. Theory Tech.*, vol. 55, no. 12, pp. 2481-2487, 2007.

[9] B. Li and Z. Shen, "Synthesis of quasi-elliptic bandpass frequency-selective surface using cascaded loop arrays," *IEEE Trans. Antennas Propag.*, vol. 61, no. 6, pp. 3053-3059, 2013.

[10] B. Li and Z. Shen, "Three-dimensional bandpass frequency-selective structures with multiple transmission zeros," *IEEE Trans. Microw. Theory Tech.*, vol. 61, no. 10, pp. 3578-3589, 2013.

[11] A. K. Rashid, Z. Shen, and B. Li, "An elliptical bandpass frequency selective structure based on microstrip lines," *IEEE Trans. Antennas Propag.*, vol. 60, no. 10, pp. 4661-4669, 2012.

[12] Z. Z. Zhao, A. X. Zhang, X. M. Chen, G. T. Peng, J. X. Li, H. Y. Shi, and A. A. Kishk, "Bandpass FSS with zeros adjustable quasi-elliptic response," *IEEE Antennas Wireless Propag. Lett.*, vol. 18, no. 6, pp. 1184-1188, 2019.

[13] M. A. Al-Joumayly and N. Behdad, "A generalized method for synthesizing low-profile, band-pass frequency selective surfaces with non-resonant constituting elements," *IEEE Trans. Antennas Propag.*, vol. 58, no. 12, pp. 4033-4041, 2010.

[14] K. Payne, K. Xu, and J. H. Choi, "Generalized synthesized technique for the design of thickness customizable high-order bandpass frequency-selective surface," *IEEE Trans. Microw. Theory Tech.*, vol. 66, no. 11, pp. 4783-4793, 2018.

[15] Z. Z. Zhao, W. Li, X. M. Chen, J. Z. Chen, H. Y. Shi, J. X. Li, S. T. Zhu, and A. X. Zhang, "Broadband angle insensitive frequency-selective surface with multiple resonant modes," *Microw. Opt. Technol. Lett.*, vol. 60, pp. 2660-2664, 2018.

[16] M. Gao, S. M. A. M. H. Abadi, and N. Behdad, "A hybrid miniaturized-element frequency selective surface with a third-order bandpass response," *IEEE Antennas Wireless Propag. Lett.*, vol. 16, pp. 708-711, 2016.

[17] M. Li and N. Behdad, "A third-order bandpass frequency selective surface with a tunable transmission null," *IEEE Trans. Antennas Propag.*, vol. 60, no. 4, pp. 2109-2113, 2012.

[18] N. Behdad, M. Al-Joumayly, and M. Salehi, "A low-profile third-order bandpass frequency selective surface," *IEEE Trans. Antennas Propag.*, vol. 57, no. 2, pp. 460-466, 2009.

[19] Q. H. Lv, C. Jin, B. C. Zhang, and R. Mittra, "Wide-passband dual-polarized elliptic frequency selective surface," *IEEE Access*, vol. 7, pp. 55833-55840, 2019.

[20] M. U. Afzal, A. Lalbakhsh, and K. P. Esselle, "Electromagnetic-wave beam-scanning antenna using near-field rotatable graded-dielectric plates," *Journal of Applied Physics*, vol. 124, no. 23, pp. 234901, 2018.

[21] A. Lalbakhsh, M. U. Afzal, and K. P. Esselle, "Multiobjective particle swarm optimization to design a time-delay equalizer metasurface for an electromagnetic band-gap resonator antenna," *IEEE Antennas Wireless Propag. Lett.*, vol. 16, pp. 912-915, 2017.

[22] A. Lalbakhsh, M. U. Afzal, K. P. Esselle, and S. L. Smith, "Low-cost nonuniform metallic lattice for rectifying aperture near-field of electromagnetic bandgap resonator antennas," *IEEE Trans. Antennas Propag.*, vol. 68, no. 5, pp. 3328-3335, 2020.

[23] A. Lalbakhsh, M. U. Afzal, K. P. Esselle, and S. Smith, "Design of an artificial magnetic conductor surface using an evolutionary algorithm," *International Conference on Electromagnetics in Advanced Applications (ICEAA)*, pp. 885-887, 2017.

[24] A. Lalbakhsh, M. U. Afzal, K. P. Esselle, and B. A. Zeb, "Multi-objective particle swarm optimization for the realization of a low profile bandpass frequency selective surface," *International Symposium on Antennas and Propagation (ISAP)*, pp. 1-4, 2015.

[25] J. S. Hong and M. J. Lancaster, *Microstrip Filters for RF/Microwave Application*. New York, NY, USA: Wiley, 2001.

[26] D. Ferreira, R. F. S. Caldeirinha, I. Cuinas, and T. R. Fernandes, "Square loop and slot frequency selective surfaces study for equivalent circuit model optimization," *IEEE Trans. Antennas Propag.*, vol. 63, no. 9, pp. 3947-3955, 2015.

[27] D. S. Wang, W. Q. Che, Y. M. Chang, K. S. Chin, and Y. L. Chow, "A low-profile frequency selective surface with controllable triband characteristics," *IEEE Antennas Wireless Propag. Lett.*, vol. 12, pp. 468-471, 2013.

[28] D. M. Pozar. *Microwave Engineering*. 3rd ed., New York, NY, USA: Wiley, 2009.

Zhengyong Yu was born in Huaian, China, in 1982. He received the B.S. degree from the Huaiyin Institute of Technology, Huaian, China, in 2006, the M.S. degree from the Nanjing University of Science and Technology, Nanjing, China, in 2008, and the Ph.D. degree from Nanjing Normal University, in 2020.

He is currently an Associate Professor and Senior Engineer in Huaian Vocational College of Information Technology. He is Jiangsu Province 333 project personnel training object, and Jiangsu Province Qing Lan project academic leader. His current research interests include fundamental electromagnetic theory, frequency selective surfaces and near-field antennas.

Wanchun Tang was born in China in 1967. He received the B.S. degree from Tsinghua University, Beijing, China, in 1990, the M.S. degree from the Nanjing University of Science and Technology, Nanjing, China, in 1995, and the Ph.D. degree from the City University of Hong Kong, Hong Kong, in 2003, all in Electrical Engineering.

He was a Full Professor with the Department of Communication Engineering, NJUST, and is currently a Specially Invited Full Professor with the Jiangsu Key Laboratory on Optoelectronic Technology, School of Physics and Technology, Nanjing Normal University, Nanjing. He has authored or coauthored over 100 journal and conference papers. His current research interests include modeling and optimization of RFIC, antennas, signal integrity, and power integrity design in package.